

Defect and density evolution under high-fluence ion irradiation of Si/SiO₂ heterostructuresF. Djurabekova *Helsinki Institute of Physics and Department of Physics, University of Helsinki, P.O. Box 43, Helsinki FIN-00014, Finland*C. Fridlund * and K. Nordlund *Department of Physics, University of Helsinki, P.O. Box 43, Helsinki FIN-00014, Finland*

(Received 21 August 2018; revised manuscript received 9 October 2019; published 3 January 2020)

We present molecular dynamics simulations of atomic mixing over a Si/SiO₂ heterostructure interface, induced by focused Ne⁺ and broad Si⁺ ion-beam irradiations, using a speed-up scheme that significantly reduces the relaxation time of the cascading recoils. To assess the qualitative reliance of the chosen method, two different potential models for Si–O, Si–Si, and O–O interactions were used: the Stillinger-Weber-like Watanabe-Samela potential and the Tersoff-like Munetoh potential. Furthermore, the molecular dynamics simulations were assessed by simulating a similar case, at a total fluence of $1 \times 10^{15} \text{ cm}^{-2}$, with the binary collision approximation. The same general atomic density profile distributions were achieved with both models; however, the binary collision approach showed shallower penetration of Si into the SiO₂ layer. Coordination analysis of the molecular dynamics results provides strong evidence that ion mixing at high fluences leads to coordination defects, which will affect the electronic properties of the structures unless removed with annealing.

DOI: [10.1103/PhysRevMaterials.4.013601](https://doi.org/10.1103/PhysRevMaterials.4.013601)

I. INTRODUCTION

The need for power-saving components is growing inevitably due to the foreseen high demand of hand-held devices connecting to the internet-of-things (IoT). The number of these devices is increasing exponentially [1]; however, miniaturization of components, which is the driving force of the development of the modern semiconductor technology, is approaching its physical limit [2]. Hence, it is necessary to search for alternative ways of progress [3]. In this regard, low-power single-electron transistors (SET) [4–7] are promising technological devices. They operate on very low electron currents, which significantly reduces the power consumption as well as undesirable heating. SETs are applicable in supersensitive electrometry, single-electron spectroscopy, generating DC currents, digital memories, etc. [8]. For realization of beneficial functionality of a SET device, it must be fully compatible with existing microelectronics. For this, one of the first requirements is that the device has to be stable at room temperature.

The principle of SETs is to allow tunneling of a single electron at a time through the gate oxide via small islands, nanodots, minimizing the current between the source and the drain [9,10]. The manufacturing process of the nanodots is not trivial, due to spatial constraints: a few nm in diameter and optimal placing between the source and the drain [5,11]. The size of the nanodot will become particularly important for enabling the single-electron effects at room temperature [11]. Devices have been demonstrated at both lower temperatures [11–13] and at room temperature [5]; however, there is not

yet a scheme for manufacturing SETs commercially at a larger scale [8].

Suggestions indicate that with careful preparation of Si/SiO₂/Si-stacked geometries, it is possible to initiate atom mixing over the layer interfaces through ion-beam irradiation. Si atoms mixed into the SiO₂ layer can, under a thermally activated annealing process, eventually conglomerate at desired locations in the SiO₂ layer [14–21]. A reproducible and manageable process to manufacture SETs can be designed by careful planning and thorough testing of each manufacturing step. In this respect, computer simulations based on reliable physical descriptions of interatomic interactions can be of great practical value. Moreover, the simulations can be used for assessing future modifications of the manufacturing process, if such are required. Since the results will be used to guide the choice of experimental parameters and conditions for a future SET structure, the accuracy of the current simulations are particularly important.

Two types of ions, Ne⁺ and Si⁺, are considered in the experiments for initiating the intensive atom mixing over the Si/SiO₂ interfaces in the stacked Si/*a*-SiO₂/Si structure [14]. The choice of Ne⁺ ions is motivated by the opportunity to use a helium ion microscope (HIM), which can provide highly focused ion-beam irradiation with a beam diameter less than 3 nm [22,23]. With this in mind, nanopillars enclosing a single nanodot, could be treated with great precision increasing the success rate of controllable positioning of the nanodot. However, irradiation with Si⁺ ions can only be done in a broad-beam regime. Nevertheless, the implanted Si atoms do not contaminate targets consisting of Si-based matrices. Atomic density profiles of unbonded Si in the buried SiO₂ layer can be used, by, e.g., kinetic Monte Carlo (kMC) [16,17,24], to predict the self-assembly of the nanodots [25].

*Corresponding author: christoffer.fridlund@helsinki.fi

Describing ion mixing induced by energetic high-fluence ion irradiation with atomistic computer simulations is challenging. Due to high computational costs, these simulations have been limited to binary collision approximation (BCA) methods extended to include the dynamic mixing of atoms, such as TRIDYN [26] and CASNEW-D [27]. However, the BCA methods are not able to take into account the modification of chemical composition and subsequent changes of energetics in the systems, which may trigger additional forces promoting mobility of atoms in the intermixing system. In principle, molecular dynamics (MD) should be able to capture these processes, although within a limited timescale. With an increasing number of atoms in the system, and a need for many consecutive cascades to achieve any observable result, the MD simulations of high-fluence ion irradiation, of covalent materials in particular, quickly become prohibitively expensive.

In this article, we present MD simulations of high-fluence ion-beam irradiation of stacked Si/SiO₂ structures with simulation parameters and geometries motivated by technological considerations and electrical current calculations [14]. The required Si/SiO₂ stack easily exceeds a million atoms, which for a sequence of high-fluence irradiation runs, places very large demands on computational capacity. To enable large length scales and allow for longer irradiation sequences, we apply the recently developed speed-up procedure [28]. We analyze the built-up damage providing in-depth information on the structural defects and interface position change in *c*-Si and *a*-SiO₂. Simpler methods such as BCA cannot provide detailed atom positions allowing this kind of precise structural defect analysis.

The article is organized as follows. In Sec. II we give a short description of the choice of potentials, preparations of the MD simulation structures, as well as the speed-up procedure. In Sec. III, we present and discuss the damage assessment of the ion-beam irradiation, as well as the advantages and shortcomings of the applied speed-up scheme for the high-fluence ion-beam irradiation.

II. METHODS

A. Interatomic potentials

In the simulations we applied two potentials widely used for simulations of radiation effects in Si–O materials. These are based on two principally different formalisms: a Tersoff-type potential by Munetoh *et al.* [29] (hereafter referred to as the *Munetoh potential*) and a Stillinger-Weber-type potential by Watanabe *et al.* [30,31], modified by Samela *et al.* [32] (hereafter referred to as the *Watanabe-Samela potential*).

Since computational efficiency is essential for the simulations, we initially chose the Munetoh potential. It has a well-optimized functional form, that is fast to evaluate computationally, and predicts bonding energy and structural properties of *a*-SiO₂ and various silica polymorphs very close to experimental data [29]. To verify the results obtained with the Munetoh potential, we performed additional simulations on a smaller system with both the Munetoh and the Watanabe-Samela potentials. The latter is less efficient; however, it has an explicit term responsible for correction of angle bonds (for more detail, see Ref. [30]). This term prevents formation of

overcoordinated defects and, hence, the potential is expected to better predict the density evolution of the system under high-fluence ion irradiation.

In previous work, we have successfully implemented both potential models in simulations of thermally equilibrated Si/SiO₂ systems [33], as well as MeV ion irradiation of SiO₂ structures [34,35]. All above-mentioned simulations show good correspondence with experimental work. However, to our knowledge, these potentials have not yet been used for the irradiation regime relevant to this work—a few tens of keV and high ion fluence.

To handle the high-energy effects of the collision cascades, both potentials were joint smoothly with the ZBL repulsive potential [36] at short distances. Electronic stopping power [37] was taken into account as a frictional force on particles with kinetic energy above 10 eV during the simulations.

B. Preparation of the MD structures

As mentioned in Sec. II A, we prepared one system with two Si/SiO₂ interfaces and one system with one single Si/SiO₂ interface. The double-interface structure was relaxed only with the more efficient Munetoh potential, while the single-interface structure was prepared with both potential models.

The lateral dimensions of the prepared cells for both the single- and the double-interface structures were chosen to fully accommodate the collision cascades, without interference from the thermostat at the borders of the simulation cell. The cell with two interfaces was 17.1 nm × 17.1 nm and the cells with a single interface were 21.7 nm × 21.5 nm and 21.8 nm × 21.8 nm, for Watanabe-Samela and Munetoh, respectively. The heavier ions used in the broad-beam irradiation simulations (Si instead of Ne) motivated the choice of slightly wider dimensions for the single-interface structures.

The thicknesses of the three layers in the double-interface system were chosen to match the experimental condition: 7 nm of the buried amorphous SiO₂ (*a*-SiO₂) and 25 nm of the top, initially crystalline Si (*c*-Si), layer. The thickness of the bottom *c*-Si layer was not relevant to the experimental condition. We chose it sufficiently thick to partially accommodate the energetic cascades that pass the lower interface. For this study, the bottom *c*-Si layer thickness, x , was set to 6 nm, as a compromise of computational efficiency and the necessity to account for backward contribution of the atom mixing in the lower interface. The geometry of the double-interface structure is shown in Fig. 1(a). We note that the top layer here is shown to be only 3 nm instead of 25 nm. This relates to a developed speed-up scheme, reducing computational time by combining BCA and MD (see Sec. II C 2). The geometry of the single-interface structures is shown in Fig. 1(b). We prepared all structures following the same preparatory steps described in Ref. [28].

To prepare a stable *a*-SiO₂ structure, we used the Wooten-Winer-Weaire method as in Ref. [33], subsequently relaxed with the Munetoh and the Watanabe-Samela potentials in the NPT ensemble for 15 ps at 300 K and 0 kbar using the Berendsen temperature and pressure controls ($\tau_T = 0.1$ ps, $\tau_p = 1.0$ ps) [38], with periodic boundary conditions (PBC) in all directions. The different potentials yielded a small difference in the sizes of the relaxed *a*-SiO₂ blocks. The

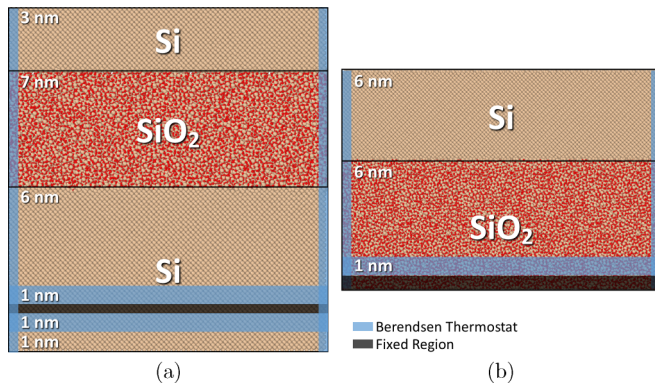


FIG. 1. The double- (a) and the single-interface (b) simulation cells and the regions of the Berendsen thermostat (blue) and the fixed atoms (black). The numbers on the structures show the thicknesses of the corresponding layers. For the lateral dimensions, see the main text. For the reasons discussed in the text, PBC were used in all directions in case (a), and in the lateral dimensions in case (b).

pair distribution functions of the a -SiO₂ are very similar (see Fig. 2), with minor discrepancies in the second and the third peaks. The inset of Fig. 2 reveals that the O–O bond lengths are distributed around the mean value more symmetrically in the Munetoh potential, while in the Watanabe-Samela potential, the tail toward larger bond lengths is longer. The Si–Si bonds have very similar distribution shapes in both potentials.

Using PBCs in the lateral directions requires that the widths of both the c -Si and the a -SiO₂ structures match perfectly, to avoid appearance of artificial mismatch stresses at the sides of the simulation cell when merged. The lattice constant of c -Si was slightly adjusted to account for the discrepancies in the lateral dimensions of the c -Si and a -SiO₂, before merging them together. The interface optimization was done in the same manner as described in Ref. [28]. The strong shock-wave coming from the merge of the structures was effectively damped during a ~ 250 ps relaxation run. We note that this method can easily be extended to any number

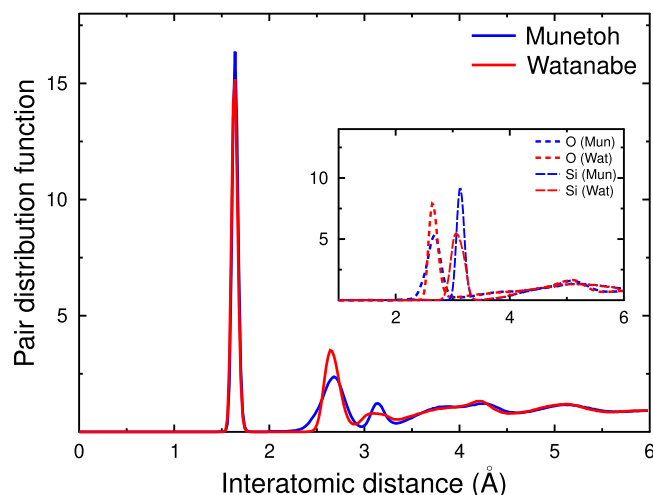


FIG. 2. The pair distribution function of the unirradiated a -SiO₂ structures obtained with both Munetoh and Watanabe-Samela potentials. The inset shows the pair distribution function separately for Si and O atoms.

of interfaces, provided that the relaxation time is adjusted accordingly.

C. Simulations of the irradiation process

1. General setup

In our simulations, we aim to understand the mechanisms of atom mixing obtained by ion irradiation of c -Si/ a -SiO₂/ c -Si heterostructures. Based on experiments, we set the ion-beam energy to 25 keV for both the focused Ne⁺ and broad Si⁺ beam [14,39]. For the sake of computational efficiency, we performed the focused ion-beam irradiation on the double-interface structure utilizing the BCA/MD speed-up procedure explained in Sec. II C 2. Simulation of the broad beam irradiation was done on the single-interface structure. In these simulations, the ions entered the open surface to allow for natural relaxation of stresses accumulated during the collision cascades. Special care was taken to ensure the same amount of deposited energy in the interface of the downscaled structures. We used SRIM [40,41] estimations of this quantity to reduce the ion energy from 25 to 3.7 keV. Although the experimental irradiation reached a fluence of $2.5 \times 10^{15} \text{ cm}^{-2}$ (corresponding to ~ 10000 consecutive ion impacts in our simulations) [14,20], we only simulated a fluence of $1.6 \times 10^{15} \text{ cm}^{-2}$ (~ 7500 impacts). This induced a sufficient disorder in the system providing strong atom mixing.

All MD simulations of the irradiation were performed in a quasi-NVE ensemble with the classical MD simulator, PARCAS [42,43]. The Berendsen thermostat [38] controlled the border atoms at the periodic boundary (see the blue regions in Fig. 1) to 300 K, and the temperature of the atoms in the collision cascade was allowed to evolve naturally. By fixing three atom layers near the bottom of the cell as shown in Figs. 1(a) and 1(b) as black regions we prevented the entire MD cell from shifting in the z -direction because of the momentum transfer from the incoming ions. The location of the fixed atoms in the double-interface cell was selected to create a small “buffer layer” between the layer with fixed atoms and the layer where the BCA cascade was introduced at the top of the cell (see Fig. 1). The temperature control was also applied in the regions near the fixed layers. The thickness of controlled border regions in the lateral directions were 0.5 and 1.0 nm around the fixed layers of atoms. The thicker cooling region at the bottom ensured that no energetic atoms were intensively interacting with the fixed layer.

All atoms with a kinetic energy greater than the displacement energy threshold (~ 50 eV [44]) were removed dynamically when reaching the Berendsen controlled region (above the fixed atoms). This was done with the assumption that the energetic atoms pass much deeper into the sample, without affecting the intermixing in the interface, and hence, could safely be removed.

In the focused ion-beam simulations, all ions initiated with BCA had the same impact position. Since the lateral size of the MD cell is rather small compared to the spread of the cascade at 22 nm, we ignored the uncertainty in the resolution of the HIM (~ 3.0 nm).

The homogeneity of the ion impacts in the broad-beam simulations was achieved by shifting the cell randomly between zero and half of the box size in both the x and y directions [45,46]. Every incoming ion was aimed at the

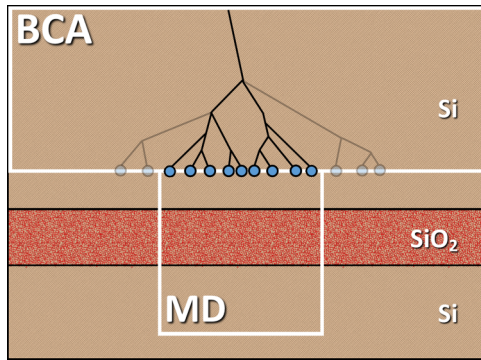


FIG. 3. The experimental layer stack of 25 nm Si on top of 7 nm SiO₂ lying on Si substrate. The simulations of the system were done in two steps: the recoil cascades were initiated with BCA in the upper Si layer, and kinetic particles with energies above 3 eV were inserted into the MD cell for simulations of the interface dynamics. The blue circles indicate the transition points of the particles.

lateral center of the simulation box 5 Å above the surface. This way the cascade always developed in the center of the simulation cell sufficiently far from the temperature controlled regions.

Furthermore, to verify the results of the high-fluence irradiation simulations, we compared the atomic density distributions from MD with profiles from TRIDYN [26]. We avoided channelling effects [47] in the initially crystalline Si layers by tilting the angle of incidence by 7° from the surface normal. For consistency, the same angle of incidence was used in the TRIDYN simulations.

2. Speed-up schemes

The size of the double-interface structure (for details see Sec. II B) was still too large for efficient MD simulations, in particular for the case of high-fluence irradiation. To cope with the problem, we adopted two speed-up schemes to reduce the computational time required for regular MD iterations.

The first scheme was designed to benefit from the efficiency of precalculating the 25 keV Ne ion cascades in the uppermost 22 nm of the 25 nm *c*-Si layer with the BCA code, CASWIN [27,35,47–49]. CASWIN does not take explicitly into account crystal structures; however, the atomic density determining the frequency of atomic collisions corresponded to the density of the *c*-Si in the MD structure. The scattering angles are calculated with the universal ZBL potential, using the “magic” formula as in SRIM [50], at every projectile’s step. This step is equal to the mean free path in the irradiated material.

The positions, energies, and directions of all recoiling atoms (including the ions) reaching a depth of 22 nm, still having kinetic energies above 3 eV, were recorded and subsequently transferred to the MD cell. The transfer was done by locating the atoms with positions closest to the recorded positions (around 3 nm above the *c*-Si/*a*-SiO₂ interface) and applying the recorded data, as done in Ref. [35]. A schematic overview of the BCA and MD combination is given in Fig. 3.

Since MD simulations take several orders of magnitude longer than BCA simulations [51], we were able to achieve an efficient reduction of computational time by explicitly

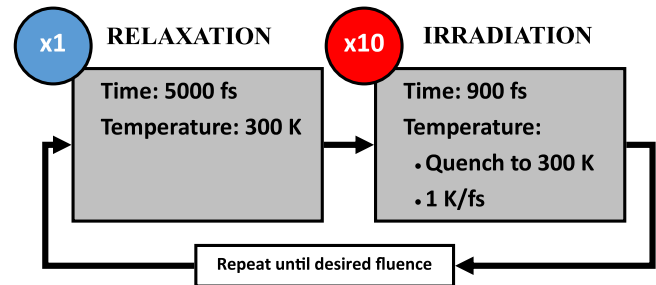


FIG. 4. Illustration of the irradiation–relaxation process. Every 10th irradiation event is followed by a longer relaxation run. This is repeated until the desired accumulated fluence is reached.

excluding the first 22 nm of the stack from the MD simulations. Nevertheless, further optimizations are needed to reach the necessary irradiation dose within reasonable time limits. As a second speed-up scheme, we optimized the time parameters of the MD simulations by shortening the duration of both the ballistic and the post-ballistic relaxation stage of the cascades, while making sure the cascades still had sufficient time to finalize the ballistic phase completely. Moreover, we incrementally increased the temperature quench rate used at the end of the relaxation: 0.1, 0.3, and 1.0 K/fs. The first of these quench rates is commonly used in MD simulations of radiation effects in materials, and allows for relaxation (or even annihilation) of transient (shallow) defects [52]. The last mentioned quench rate (1.0 K/fs) removes the heat very quickly, practically freezing the atoms in the current positions, which leads to the possibility of artificial buildup of local stresses within the structure.

We noted from test runs that this procedure leads to a cumulative temperature rise of ~180 K during the cascades. Hence, longer relaxation time between the subsequent cascades is needed. In our simulations, we used the following optimized parameters (stepwise) to speed-up the calculations: (1) cascade development for 500 fs, (2) temperature quench for ~200 fs at the rate ~1.0 K/fs, and (3) relaxation run at 300 K for ~200 fs. Every 10th cascade event was followed by a 5 ps relaxation run. This scheme is illustrated in Fig. 4. To benchmark this speed-up scheme, we performed full MD simulations of the focused ion-beam irradiation. In these runs, the cascades were simulated for 6.5 ps before quenching the temperature with a rate of 0.1 K/fs.

Unfortunately, neither scheme allows for the thermally activated defect migration and relaxation between collision cascades. However, the calculations of the ballistic phase of the cascades defining the efficiency of the atom mixing is fully captured. Moreover, the relaxation after every 10th ion irradiation event is sufficient for atoms to assume better equilibrated positions in the structure, especially in the regions with the highest local density.

III. RESULTS AND DISCUSSION

A. Focused ion-beam irradiation of the double-interface structure

The state of the stacked double-interface structure after a fluence of $1.6 \times 10^{15} \text{ cm}^{-2}$ (7500 ions) can be seen in Fig. 5. Figure 5(a) shows the distribution of the species in the

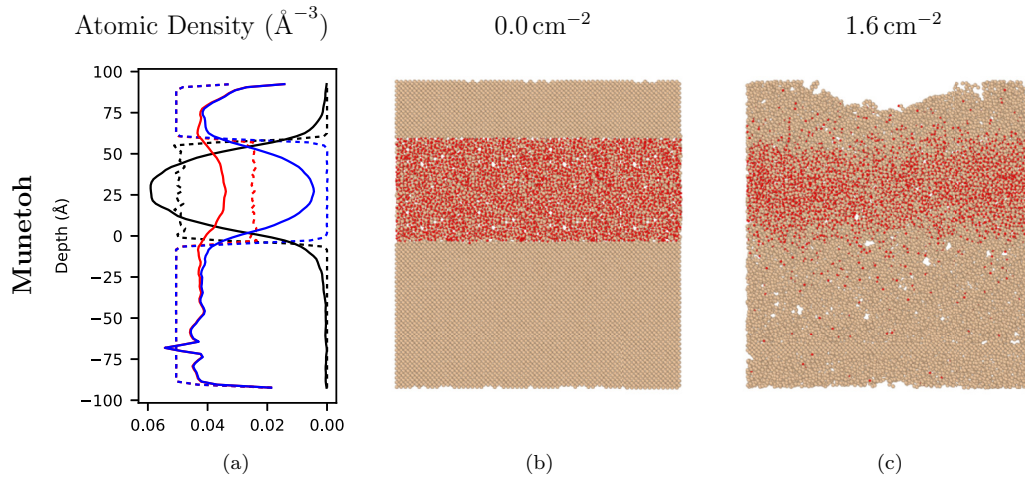


FIG. 5. Ion mixing in the double interface Si/*a*-SiO₂/Si structure. (a) Atomic density profiles before (dotted lines) and after 7500 cascade events (solid lines) for all atom types present in the system. Black color shows the density profile of the O atoms, red color shows the profiles of the stoichiometric Si atoms. The excess of the Si atoms with respect to the stoichiometric Si content in SiO₂ is shown in blue color. (b) The snapshot of the initial structure with atomically sharp interfaces [dashed lines in (a)]; (c) the snapshot of the structure after the irradiation fluence of $1.6 \times 10^{15} \text{ cm}^{-2}$ [solid lines in (a)].

simulation cell before and after irradiation, while Figs. 5(b) and 5(c) show the corresponding illustrations of the atomic structures. In Fig. 5(a), we analyze the atomic density of Si and O separately as a function of depth (perpendicular to the interfaces). There may be lateral variations in the density caused by inhomogeneous ion mixing as a result of the focused ion beam. These variations are practically impossible to capture at the insertion depth due to the lateral spread of the beam, greatly superceding the lateral width of the simulation box.

The dynamic evolution of excess Si atoms is demonstrated by calculating the content of stoichiometric Si (Si bonded to two O atoms) in the *a*-SiO₂. For consistency, all atoms in the Si layer are considered to be “excessive,” since initially there are no O atoms in this layer. These profiles are shown in blue in all the figures in this section.

During ion irradiation we note a decrease in the thickness of the SiO₂ layer. The decrease can be explained by intensive atom mixing: the atoms displaced in the cascades move forward to deeper layers, while O atoms also move backwards into the upper Si layer, but less intensively. This explains the slightly asymmetric distribution of O concentration toward the upper and lower Si layers. However, we still observe an abnormal increase in density of the SiO₂ layer. The atomic density of O and Si (black and red solid lines) is much higher after 7500 ions, compared to the initial atomic densities of the corresponding species (dashed lines).

In these simulations, we see formation of voids in the region where the BCA cascades were introduced into the MD cell. The appearance of these voids is fairly natural given the circumstances: each BCA cascade reaching the transition layer may involve dozens of energetic recoils. These recoils are introduced nearly simultaneously (there is no information about the temporal order of the produced recoils). The concentrated transferred momentum gives cause to strong irreversible displacements within the MD time scale. After many ions, this inevitably leads to formation of an internal surface under the

region where the BCA cascades are introduced in the upper Si layer. Although the voids in our simulations may be the result of insufficient relaxation between the cascades, we still report them here to demonstrate that similar processes may occur in experiments as well. Hence, we emphasize that the surface depression may be caused not only by sputtering, but also by atom displacement under prolonged focused ion-beam irradiation.

The overall Si-to-O atom ratio remains close to stoichiometric, confirming that the obtained results can be used to predict the ion-induced atom mixing in Si/SiO₂ structures. However, the appearance of a void with constant volume presents a disturbing trend in the evolution of the atomic densities. We observe a gradual densification of the *a*-SiO₂ layer with increasing ion fluence. The final compression of $\sim 20\%$ is unexpectedly high. Experimentally, it is known that prolonged irradiation of *a*-SiO₂ indeed may lead to densification, but not higher than $\sim 2\%$ [53–55].

We note here that the reduction in atomic density of Si (from $\sim 0.05 \text{ \AA}^{-3}$ to $\sim 0.04 \text{ \AA}^{-3}$, see the left column in Fig. 5), is expected and relates to the amorphization of *c*-Si and relocation of Si atoms into the SiO₂ layer.

B. Broad ion-beam irradiation of the single-interface structures

To understand the reasons of the densification, we simplified the approach and simulated the broad 3.7 keV Si irradiation on a smaller Si/SiO₂ structure. We removed the BCA step and opened the *z* surface allowing for natural relaxation of induced stresses. The ion energy was reduced to emulate the same amount of energy deposition in the interface region as in the larger simulation. We performed these simulations with both of the aforementioned potential models to validate the sensitivity of the obtained results to the choice of the model of interatomic interactions (for details see Sec. II A). An in-depth coordination analysis of the irradiated structures was performed to elucidate possible reasons of the densification

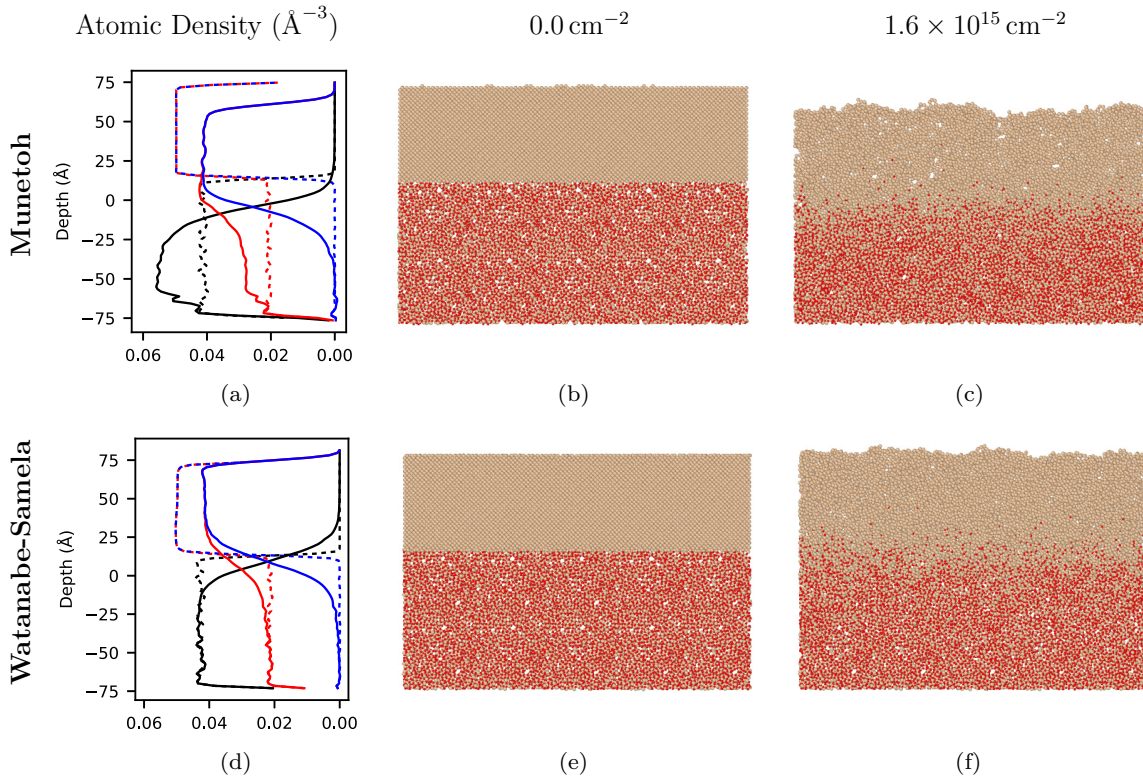


FIG. 6. Results of the MD simulations of the single interface system. On the left (a and d) are the atomic density profiles for all atom types present in the system, the colors are the same as in Fig. 5; in the center (b and e) are the interfaces before any irradiation (dashed lines in the profile figures); and on the right (c and f) are the interfaces after an irradiation dose of $1.6 \times 10^{15} \text{ cm}^{-2}$ (~ 7500 ions, solid lines in the density profiles).

process found during the prolonged irradiation simulations. Figure 6 shows the results of the 3.7 keV Si ion irradiation in the same manner as Fig. 5. The top row of Fig. 6, i.e., Figs. 6(a)–6(c), shows the results obtained with the Munetoh potential and the row below [Figs. 6(d)–6(f)] shows the results from the Watanabe-Samela potential. In these figures we see that the atoms involved in cascades actively intermix around the initially sharp interface, rendering it more blurry with increasing fluence. Figure 6 shows that the general interface broadening is almost identical in both potentials, which is understandable, since intermixing takes place during the ballistic phase of the cascade evolution described mainly by the ZBL potential [36]. Overall, the atomic density profiles obtained in the single-interface structure (broad ion-beam irradiation) compare very well with those obtained in the double-interface structure (focused ion-beam irradiation), which is well seen in Figs. 5 and 6. However, more detailed comparison of the distributions in Figs. 6(a) and 6(d) reveals that the amount of excess Si (blue curves) is much higher at the interface in the Munetoh potential. The profiles from the Watanabe-Samela potential are smoother and the overdensification of the SiO_2 layer and underdensification of the Si layer are less dramatic, although these features do not disappear completely. We see a slight depression of the surface with both potentials [see Figs. 6(c) and 6(f)], and a greater increase in density of the SiO_2 layer with the Munetoh potential. The good agreement between the two models provides a mutual verification of the simulated results.

We compared the results from the Watanabe-Samela potential simulations directly with the results from the BCA code TRIDYN [26]. In the latter, the dynamic evolution of the density profiles with increasing fluence is predicted only through ballistic collisions of atoms described by the ZBL potential. However, it is not possible to follow exact dynamics of the evolution of component profiles, since there are no “real” atoms present in the BCA system. Figure 7 shows the atomic density profiles obtained by both TRIDYN and PARCAS. In the comparison, we aligned the initial positions of the Si/ SiO_2 interfaces in both models. We notice that the Si/ SiO_2 interface does not change position in the BCA simulations, only a broadening effect can be observed. However, in the MD simulations the interface shows a small downwards-directed shift, compared to the initial state. This shift is explained by a small densification of the SiO_2 layer and the momentum transferred by the incoming ions to the target atoms. We note that the MD profiles are broader and indicate intermixing of Si atoms deeper into the SiO_2 layer compared to the BCA model.

C. Coordination analysis of the atoms in the single-interface structures

As we see in Fig. 6, the atomic density of O raises above equilibrium in the SiO_2 layer during the broad-beam irradiation. Naturally, irradiated structures are expected to densify during irradiation due to interstitials forming in the cascades [53–58]. Interstitials and vacancies in covalent materials, such as Si and SiO_2 are energetically unfavorable and

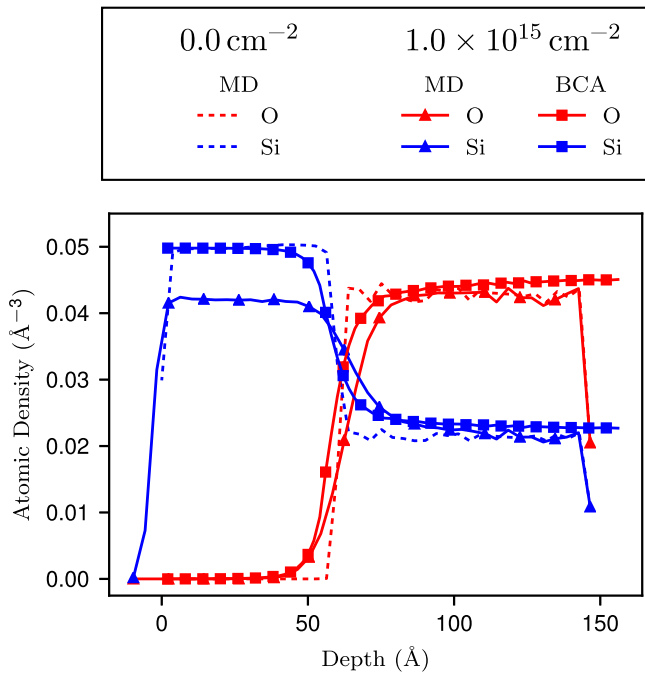
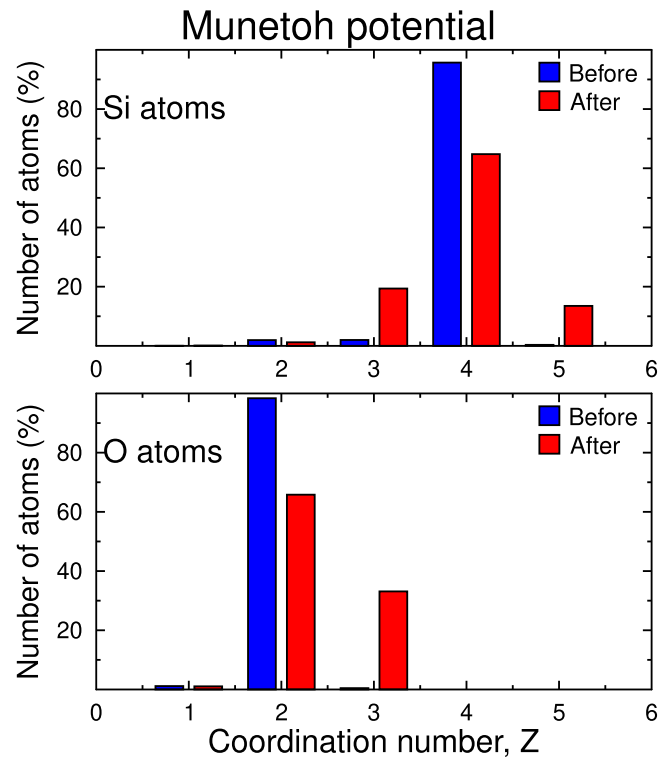


FIG. 7. Comparison of the atomic density profiles between the two simulation models. The BCA profiles were simulated with TRIDYN on a semi-infinite Si/SiO₂ system, and the MD profiles were simulated with PARCAS and the speed-up model described in Sec. II C. The profiles are aligned on the Si/SiO₂ interface to give a good point of reference between them. The profiles shown here are from a total fluence of $1 \times 10^{15} \text{ cm}^{-2}$ (~ 5000 ions). For a reference point of view, the profiles of the unirradiated MD structure are presented with dashed lines.

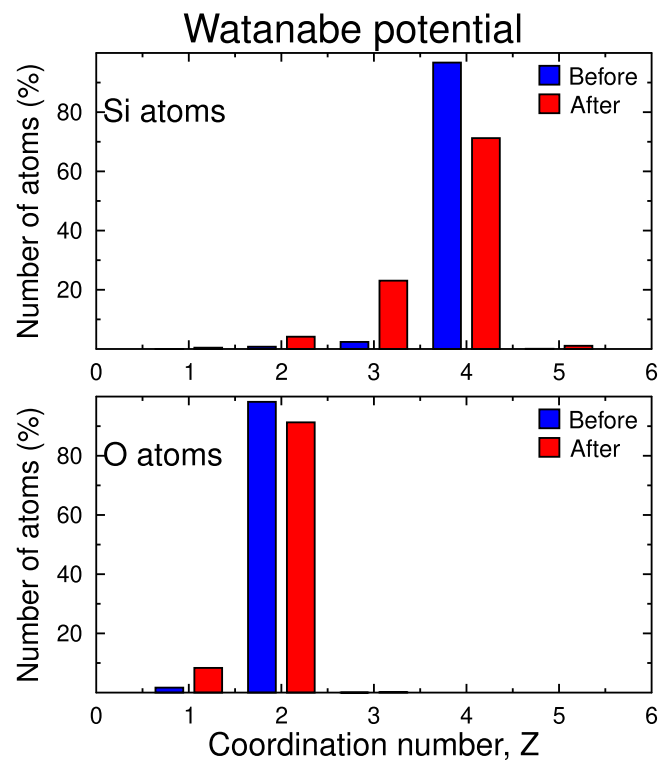
tend to partially recombine during experimental time scales (of the order of seconds). This greatly reduces the rate of defect accumulation during subsequent collision cascades in the materials [59,60]. However, in MD time scales, these defects may survive, effectively increasing the level of disorder and hence the expected atom mixing. This is why it is important to analyze the nature of the produced defects through coordination analysis [33]. Atoms with too many neighbors (overcoordinated atoms) can be associated with the presence of interstitials, while a deficit of neighbors suggests the presence of vacancies. Interstitials and vacancies near each other will eventually recombine and adjust to more favorable locations. Moreover, the balance of over- and undercoordinated atoms along with the pair distribution function may shed light on possible artifacts leading to the extreme densification observed in the simulations.

We used the following element-specific cutoff radii in the pair distribution function: $r_{\text{Si-O}} = 2.0 \text{ \AA}$, $r_{\text{Si-Si}} = 2.7 \text{ \AA}$, and $r_{\text{O-O}} = 2.0 \text{ \AA}$ (see Fig. 2). In the Watanabe-Samela potential O-O interactions are described as purely repulsive, while in the Munetoh potential, formation of O-O bonds is possible ($a_{\text{O-O}} = 1.5 \text{ \AA}$ [29]).

Figure 8 shows the distribution of coordination numbers for O and Si separately, both at a fluence of 0 cm^{-2} (before)



(a)



(b)

FIG. 8. Coordination number evolution for both Si and O atoms before and after a fluence of $1.6 \times 10^{15} \text{ cm}^{-2}$, for both (a) Munetoh and (b) Watanabe-Samela potentials.

TABLE I. Analysis of coordination defects in the single-interface structure simulated with the Munetoh potential, after the final fluence of $1.6 \times 10^{15} \text{ cm}^{-2}$. The Si–Si, Si–O, O–Si, and O–O bonds are presented separately. N_b^{x-y} indicates the average amount of bonds going from type x to type y (e.g., $x = \text{Si}$ to $y = \text{O}$, the total is defined by Z); $\langle d_b^{x-y} \rangle$ shows the average bond length between the types, given in Å; and $\frac{N_Z^x}{N_{\text{total}}^x}$ is the fraction of type x with coordination number Z , with respect to all atoms of type x , given in percent. $\langle Z \rangle$, in the subheader, shows the average coordination number for the given species, and the errors are the standard deviation of the mean.

Z	$\langle N_b^{x-\text{Si}} \rangle$	$\langle d_b^{x-\text{Si}} \rangle$	$\langle N_b^{x-\text{O}} \rangle$	$\langle d_b^{x-\text{O}} \rangle$	$\frac{N_Z^x}{N_{\text{total}}^x}$
Coordination defects of $x = \text{Si}$ atoms: $\langle Z \rangle = 3.94 \pm 0.65$					
2	1.34 ± 0.88	2.33 ± 0.06	0.66 ± 0.88	1.65 ± 0.07	1.2%
3	2.07 ± 1.23	2.35 ± 0.07	0.93 ± 1.23	1.67 ± 0.06	19.4%
4	2.56 ± 1.76	2.38 ± 0.07	1.44 ± 1.76	1.68 ± 0.06	64.8%
5	2.24 ± 2.34	2.43 ± 0.07	2.76 ± 2.34	1.71 ± 0.06	13.5%
Coordination defects of $x = \text{O}$ atoms: $\langle Z \rangle = 2.32 \pm 0.5$					
1	0.98 ± 0.13	1.67 ± 0.05	0.02 ± 0.13	1.53 ± 0.06	1.1%
2	1.97 ± 0.16	1.66 ± 0.05	0.03 ± 0.16	1.53 ± 0.05	65.8%
3	2.98 ± 0.15	1.73 ± 0.05	0.02 ± 0.15	1.56 ± 0.05	33.1%

and $1.6 \times 10^{15} \text{ cm}^{-2}$ (after). We clearly see that before irradiation (blue bars) there are very few coordination defects, and almost all Si atoms are fourfolded, while all O atoms are twofold bonded in both potentials. After irradiation, we see that Si atoms still retain to large extent the correct fourfold coordination in both potential models. In the Watanabe-Samela potential, the defects are mainly undercoordinated with a few atoms gaining one extra neighbor. In the Munetoh potential, the under- and overcoordinated atoms are closer in the amount with only minor dominance of the undercoordinated atoms. Such a behavior is explained by the specifics of the chosen potentials. The Watanabe-Samela potential handles overcoordinated defects with an additional energy penalty term (for details see Ref. [30]). It is clear that the bond-order term of the Tersoff formalism, also found in the Munetoh potential, is not sufficiently efficient to prevent formation of overcoordinated atoms in the far-from-equilibrium condition in the studied system. Extra relaxation time is needed to equilibrate the condition. Defect analysis for O atoms reveals practically no defects in the Watanabe-Samela potential [see lower panel in Fig. 8(b)], while the attractive part of O–O interactions may be responsible for the majority of the 30% overcoordinated O atoms in the Munetoh potential. We expect these numbers to contribute greatly to densification of the α -SiO₂ layer under prolonged irradiation.

Tables I and II provide detailed information about the coordination defects for both Si and O atoms in the single-interface structure (for both potential models) after completing the irradiation. The first column contains the coordination number (Z) of the examined atom type x (Si or O, specified in the subheaders of the table). This is followed by the average counts of the Si neighbors ($\langle N_b^{x-\text{Si}} \rangle$ in column 2) or the O neighbors ($\langle N_b^{x-\text{O}} \rangle$ in column 4). We also show the corresponding average bond length ($\langle d_b^{x-\text{Si}} \rangle$ in column 3 and $\langle d_b^{x-\text{O}} \rangle$ in column 5). The last column shows the percentage of the atoms of the type x and the coordination number Z with respect to all atoms of the same type. The coordination number specified in the subheader is averaged over all atoms.

We observe a consistent general tendency of defect evolution predicted by both potentials when comparing the tables. The average coordination number for Si in both potentials is less than four (3.94 and 3.68 in Munetoh and Watanabe-Samela, respectively). Since these simulations were done on a cell with open surface, the sputtering may affect the average coordination number of Si atoms in the top Si layer. We reduced this effect in the analysis by excluding the surface roughened by the sputtering. However, we cannot exclude the effect of sputtering completely, as the sputtered atoms may leave vacancies deep below the surface, increasing the number of undercoordinated atoms in the top layer.

TABLE II. The same analysis as in Table I, but for the Watanabe-Samela potential.

Z	$\langle N_b^{x-\text{Si}} \rangle$	$\langle d_b^{x-\text{Si}} \rangle$	$\langle N_b^{x-\text{O}} \rangle$	$\langle d_b^{x-\text{O}} \rangle$	$\frac{N_Z^x}{N_{\text{total}}^x}$
Coordination defects of $x = \text{Si}$ atoms: $\langle Z \rangle = 3.68 \pm 0.6$					
2	1.68 ± 0.67	2.45 ± 0.08	0.32 ± 0.71	1.64 ± 0.03	4.2%
3	2.41 ± 1.05	2.44 ± 0.08	0.59 ± 1.05	1.64 ± 0.03	23.1%
4	2.4 ± 1.75	2.44 ± 0.06	1.6 ± 1.75	1.64 ± 0.03	71.2%
Coordination defects of $x = \text{O}$ atoms: $\langle Z \rangle = 1.9 \pm 0.3$					
1	1.00 ± 0.00	1.62 ± 0.03			8.3%
2	2.00 ± 0.00	1.64 ± 0.03			91.3%
3	3.00 ± 0.00	1.74 ± 0.05			0.2%

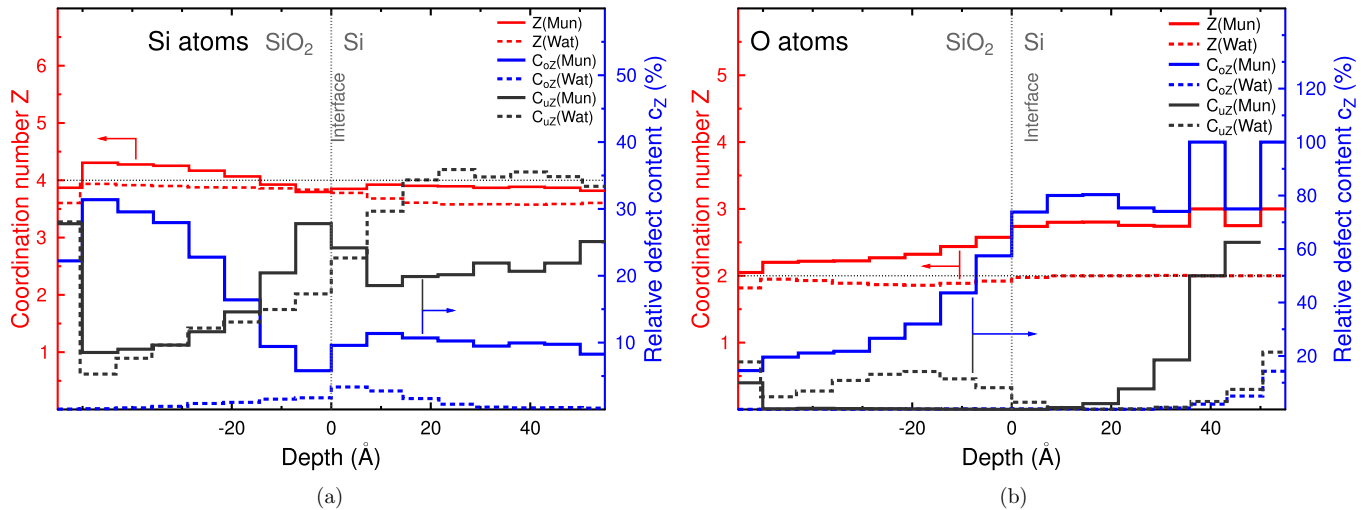


FIG. 9. Analysis of the coordination defect distributions, for (a) Si and (b) O atoms, in the irradiated single-interface structure (for both the Munetoh (Mun) and the Watanabe-Samela (Wat) potentials). oZ stands for the overcoordinated and uZ the undercoordinated atom numbers. The thin vertical line in both figures indicates the initial position of the interface, and the top surface is toward the right. The left y axis (red) shows the average coordination number distribution. The thin horizontal line in (a) and (b) guides the eye to the theoretical coordination number of Si and O (4 and 2, respectively). The right y axis (blue) shows the content of under- and overcoordinated atoms as percentage of total number of atoms of the same type ($c_{oZ,uZ} = N_{Si,O}^{oZ,uZ}/N_{Si,O}$). The red and blue arrows guide the eye to the corresponding y axis. The distributions are calculated at the same fluence ($1.6 \times 10^{15} \text{ cm}^{-2}$) as the data in Tables I and II.

In both potentials, the initial relative content of bonds to Si and O neighbors for Si atoms are $\langle N_b^{Si-Si} \rangle \approx 2.6$ and $\langle N_b^{Si-O} \rangle \approx 1.4$. These are the contributions found in the pure Si and α -SiO₂ layers, respectively. The ratio received after the irradiation is more dramatically modified in the Munetoh potential. We see that the number of Si–O bonds for the fourfold coordinated Si atoms is increased stronger in the Watanabe-Samela potential, indicating stronger intermixing, while in the Munetoh potentials both the Si–Si and Si–O bonds only slightly deviate from the initial values. In this potential, the intermixing of Si atoms into the SiO₂ is mainly observed through the bond content of the overcoordinated Si atoms. Since the number of Si–Si bonds was higher than Si–O bonds (2.6 versus 1.4), a similar amount of both bonds for overcoordinated Si atoms reveals an increase of Si in the SiO₂ layer and increase of O in the Si layer. The change of the content of the bonds for the undercoordinated Si atoms is less informative, as both numbers reduce somewhat proportionally to their initial values. In the Watanabe-Samela potential, the reduction of the content of the Si–Si bonds is less dramatic compared to the Munetoh potential, while the Si–O bonds drops more than half. This result shows that O atoms in the Watanabe-Samela potential are more “active” due to the repulsive nature of O–O interactions.

Coordination analysis for O atoms confirms the tendency toward overcoordination seen in Fig. 8(a). No overcoordinated defects are observed in the Watanabe-Samela potential, while in Munetoh potential the number of overcoordinated O atoms amounts to 33%. Mainly they form in the Si layer, since the content of O–Si bonds is prevailing; however, we see formation of a few O–O bonds as well. These form at the interatomic distance $\sim 1.5 \text{ \AA}$, which is given by the Munetoh potential [29]. The data in the table shows that there is a small fraction (0.02 of 1.1%) of molecular oxygen not bound to any

other atoms. Formation of molecular dimers is a well known effect, e.g., in irradiated GaN [61,62], and hence observing it in irradiated silica is reasonable.

Furthermore, we analyze the distribution of coordination defects through the simulation cells. In Fig. 9, we show the distribution of atom coordination through the simulation cell. The histograms are built by averaging the value of the coordination number of the atoms found in the given slab (left y axis) and the percentage of overcoordinated (solid lines) and undercoordinated (dashed lines) atoms of a given type with respect to the total number of atoms of the same type found in the same slab (right y axis). These graphs illustrate the dynamics of intermixing in different layers. We see that the average coordination number for Si does not change with depth. In Watanabe-Samela potential, $\langle Z \rangle$ of Si atoms is always less than four, while in the Munetoh potential, Si atoms become overcoordinated closer to the bottom of the cell. Slight overcoordination in the Watanabe-Samela potential is observed only near the interface, where the system experienced the strongest effect of intermixing. The distribution of undercoordinated Si atoms in the cell is more equilibrated, especially in the Munetoh potential. This observation is in line with the conclusion derived from Table I, i.e., the content of the Si–Si and Si–O bonds reduced proportionally for the three- and twofold coordinated Si atoms. In the Watanabe-Samela potential, the presence of the surface may have played a role in the stronger increase of the undercoordinated Si atoms in the Si layer. It is clear that both potentials are suitable for simulations of high-fluence irradiation of pure Si structures, however, the Munetoh potential is less suitable for the rapid temperature quench, as the soft terms of the bond-order function require longer times to equilibrate the system.

The depth distribution of the coordination defects of O atoms indicates more severe problems with respect to the

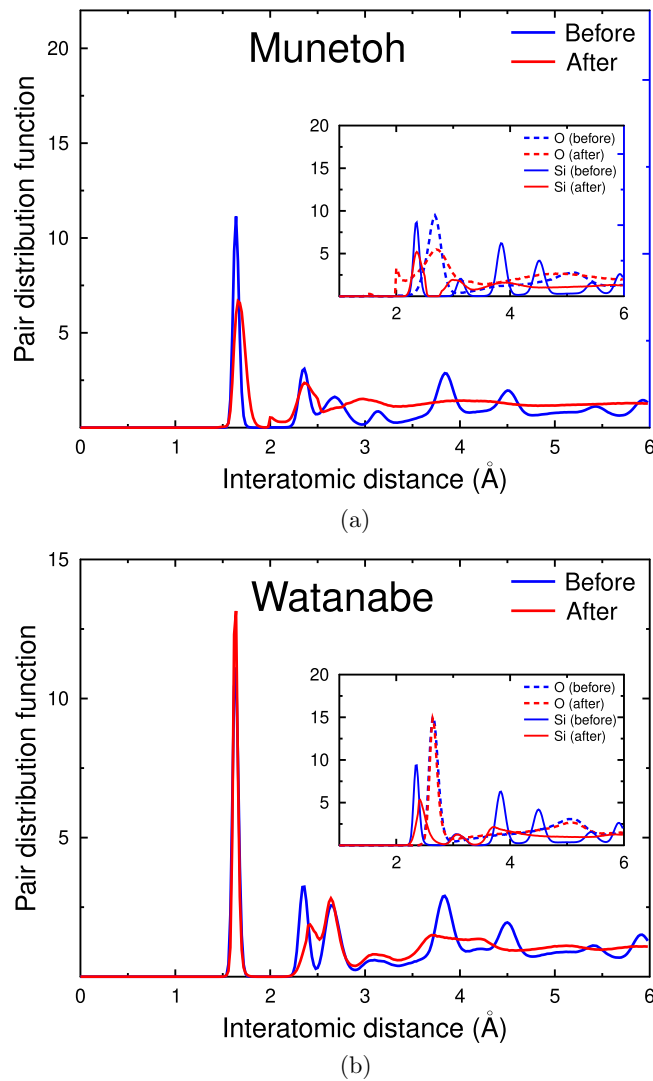


FIG. 10. Pair distribution functions of the single-interface structure before and after irradiation ($1.6 \times 10^{15} \text{ cm}^{-2}$ fluence), obtained with both (a) Munetoh and (b) Watanabe-Samela potentials. The insets show the partial pair distribution functions separately for Si and O atoms.

applicability of the Munetoh potential for simulations of high-fluence ion irradiation of SiO_2 systems. Overcoordination of O atoms is increasing toward the Si layer. It is clear that the O atoms, which were moved toward the Si layer in collision cascades got stuck between the atoms. Close to the surface we detect some undercoordinated O atoms as well, which are likely to appear due to the sputtering effect, nevertheless, the average coordination number of these atoms is almost three. This tendency is also strong in the interface region where atoms intermix. Such strong overcoordination of O atoms contributes to overdensification of the SiO_2 layer creating a strong artifact with respect to the density in the simulation results.

Pair distribution functions for the single-interface structure (for both potentials), before and after the irradiation, are shown in Figs. 10(a) and 10(b). The figure insets show the partial Si and O radial distribution functions. The distributions

obtained with both potentials show some clear differences. For example, we see that the Si–Si bonds in the Munetoh potential are practically unaffected by irradiation (the position of the Si–Si peak does not shift). However, in the Watanabe-Samela potential, the Si–Si bonds are slightly extended on average (from around 2.37 \AA to around 2.5 \AA), almost merging with the O–O peak. This indicates that in the Watanabe-Samela potential Si–Si bonds are affected stronger than the O–O bonds. The O–O peak in the Watanabe-Samela potential remains intact, while the behavior of O–O peak in the Munetoh potential is more remarkable. We see that the initial single O–O peak in the Munetoh potential (located around 2.7 \AA) splits into two distinct peaks after the irradiation: one being at a dramatically shorter distance than the original one, just above 2 \AA . It is clear that intensive irradiation causes displacements of large amounts of atoms. These atoms are not able to return to the potential wells described by the potential, developed for equilibrium or near-equilibrium condition, even during long relaxations, as there is no interaction between O–O atoms at distances beyond 2 \AA . Apparently, these O atoms are able to rearrange inside the random Si–O network, filling in the large empty spaces between the atoms of the matrix. Prolonged relaxation with this potential was not able to reduce the density of the SiO_2 layer, which also corroborates the assumption of the effect of a short O–O cut-off distance in the potential. This behavior can be easily overlooked at low-fluence irradiations, or in simulations at thermodynamic equilibrium, i.e., situations when the content of formed defects is dilute in otherwise undamaged structures.

The O–O pair distribution function has a tiny peak to the left of the 2 \AA mark [see the inset of Fig. 10(a)]. The Munetoh potential causes about 3% of the O atoms to have mixed bonds, these have on average more than one O neighbor bound on short ranges (1.53 \AA). Some of these bonds appear for the threefold coordinated O atoms as well, but at larger distance and in much smaller quantity. This finding confirms the conclusion of possible formation of O–O bonds in Table I. However, we see that these are not isolated molecules (since these atoms have on average almost a full bond to Si). Such a configuration is known as a peroxy defect in quartz [63] and can be metastable on long time scales.

Overall, we find the defects formed by both potentials very similar. The tendency for overdensification is more prominent with the Munetoh potential, while the energy penalty terms in the Watanabe-Samela potential promote expansion of the lattice to accommodate the displaced defects during irradiation. In any case, a full relaxation of the densities is infeasible within the MD time scale, as they are mostly driven by longer term diffusion processes. The O–O interactions become more important in the process of high-fluence ion irradiation. Since the Munetoh potential clearly overestimates the number of overcoordinated atoms, while O interaction in the Watanabe-Samela potentials does not allow for formation of O–O bonds, we conclude that better O–O interactions within silica potentials are needed to enable a more realistic description of O–O bond formation. However, the direct atom mixing as an immediate result of ion irradiation is well captured by the present simulations, and provide a better understanding of the extent of the effect into the interfacing layers compared to BCA results.

The speed-up algorithm causes natural over-estimation of the atomic densities within the SiO₂ layer. However, the analysis shows that the densification is not only an artifact of short relaxation times, but also due to limitations of the interatomic potentials. Some interactions are not incorporated in the available potentials. The not so crucial O–O interactions become more decisive for accurately describing the dynamics of structural changes further away from the equilibrium conditions.

IV. CONCLUSIONS

We presented molecular dynamics (MD) simulations of high-fluence ($1.6 \times 10^{15} \text{ cm}^{-2}$) ion induced atom mixing in heterogeneous multi-layered Si/SiO₂ nanostructures, during focused and broad ion-beam irradiation.

To achieve the high fluence, we developed a speed-up scheme enabling atomistic simulation of high-fluence ion irradiation with MD. The collision cascades are initiated with binary collision approximation (BCA), within the homogeneous top layer, and all energetic recoils reaching the threshold depth above the first Si/SiO₂ interface are transferred into MD based on location and energy. Every consecutive cascade was followed by a short thermal relaxation. To prevent accumulation of stresses and to allow for defect relaxation, a single longer relaxation was run after every 10th ion cascade. The simulations of the focused ion-beam irradiation showed formation of a void/crater at the impact area, indicating the effect of momentum transfer which hammers atoms into the surface and together with sputtering, will contribute to form craters during the prolonged focused irradiation.

The results of the MD simulations were verified by two very different interatomic potentials, the Stillinger-Weber-like

Watanabe-Samela potential and the Tersoff-like Munetoh potential. The use of the latter led to strong densification of the SiO₂ layer. Detailed analysis of the coordination defects revealed a strong tendency toward overcoordination of O atoms within the Munetoh potential. Moreover, the short potential cutoff for O–O interactions led to formation of a stable artificial peak in the O–O pair distribution function, not possible to relax away. Based on the results of this work, we conclude that the more optimized Munetoh potential, is less suitable for the high-fluence simulations of Si/SiO₂ systems.

This provides a strong evidence that ion mixing at high fluences leads to coordination defects, that eventually will affect the electronic properties of the structures unless removed with annealing. Although, the potentials behaved somewhat differently, the most important results regarding the magnitude of the ion mixing, such as the content of excessive Si atoms in the SiO₂ matrix, were found to not depend on the choice of interatomic potential.

ACKNOWLEDGMENTS

This project has received funding from the European Union's Horizon 2020 research and innovation programme under Grant Agreement No. 688072. The views and opinions expressed herein do not necessarily reflect those of the European Commission. We thank the Finnish Grid and Cloud Infrastructure (FGCI), urn:nbn:fi:research-infras-2016072533, and CSC–IT Center for Science, Finland, for computational resources. Special thanks to prof. Wolfhard Möller at Helmholtz-Zentrum Dresden-Rossendorf for the TRIDYN simulations and insightful discussions.

-
- [1] D. L. Feldheim and C. D. Keating, *Chem. Soc. Rev.* **27**, 1 (1998).
- [2] J. Meindl, *Proc. IEEE* **89**, 223 (2001).
- [3] Y. Takahashi, Y. Ono, A. Fujiwara, and H. Inokawa, *J. Phys.: Condens. Matter* **14**, R995 (2002).
- [4] M. A. Kastner, *Rev. Mod. Phys.* **64**, 849 (1992).
- [5] K. Matsumoto, M. Ishii, K. Segawa, Y. Oka, B. J. Vartanian, and J. S. Harris, *Appl. Phys. Lett.* **68**, 34 (1996).
- [6] L. Guo, *Science* **275**, 649 (1997).
- [7] S. Lee, Y. Lee, E. B. Song, and T. Hiramoto, *Nano Lett.* **14**, 71 (2014).
- [8] K. Likharev, *Proc. IEEE* **87**, 606 (1999).
- [9] D. Goldhaber-Gordon, J. Göres, M. A. Kastner, H. Shtrikman, D. Mahalu, and U. Meirav, *Phys. Rev. Lett.* **81**, 5225 (1998).
- [10] M. A. Kastner, D. Goldhaber-Gordon, H. Shtrikman, D. Mahalu, D. Abusch-Magder, and U. Meirav, *Nature* **391**, 156 (1998).
- [11] H. Ishikuro and T. Hiramoto, *Appl. Phys. Lett.* **71**, 3691 (1997).
- [12] H. Matsuoka and S. Kimura, *Appl. Phys. Lett.* **66**, 613 (1995).
- [13] A. Fujiwara, Y. Takahashi, K. Murase, and M. Tabe, *Appl. Phys. Lett.* **67**, 2957 (1995).
- [14] Ions4SET Website, <http://www.ions4set.eu/> (2019).
- [15] P. Novikov, K.-H. Heinig, A. Larsen, and A. Dvurechenskii, *Nucl. Instrum. Methods Phys. Res. Sect. B* **191**, 462 (2002).
- [16] T. Müller, K.-H. Heinig, and W. Möller, *Appl. Phys. Lett.* **81**, 3049 (2002).
- [17] T. Müller, K.-H. Heinig, and W. Möller, *Mater. Sci. Eng. B* **101**, 49 (2003).
- [18] L. Röntzsch, K.-H. Heinig, and B. Schmidt, *Mater. Sci. Semicond. Process.* **7**, 357 (2004).
- [19] L. Röntzsch, K.-H. Heinig, B. Schmidt, A. Mücklich, W. Möller, J. Thomas, and T. Gemming, *Phys. Status Solidi* **202**, R170 (2005).
- [20] B. Schmidt, K.-H. Heinig, L. Röntzsch, T. Müller, K.-H. Stegmann, and E. Votintseva, *Nucl. Instrum. Methods Phys. Res. Sect. B* **242**, 146 (2006).
- [21] E. A. Mikhantiev, I. G. Neizvestny, S. V. Usenkov, and N. L. Shwartz, *Comput. Mater. Sci.* **90**, 99 (2014).
- [22] *Helium Ion Microscopy*, edited by G. Hlawacek and A. Götzhäuser, NanoScience and Technology (Springer International Publishing, Cham, 2016).
- [23] G. Hlawacek, V. Veligura, R. van Gastel, and B. Poelsema, *J. Vac. Sci. Technol. B* **32**, 020801 (2014).
- [24] T. Müller, K.-H. Heinig, W. Möller, C. Bonafos, H. Coffin, N. Cherkashin, G. B. Assayag, S. Schamm, G. Zanchi, A. Claverie, M. Tencé, and C. Colliex, *Appl. Phys. Lett.* **85**, 2373 (2004).
- [25] S. Ilday, F. Ö. Ilday, R. Hübner, T. J. Prosa, I. Martin, G. Nogay, I. Kabacelik, Z. Mics, M. Bonn, D. Turchinovich, H. Toffoli, D.

- Toffoli, D. Friedrich, B. Schmidt, K.-H. Heinig, and R. Turan, *Nano Lett.* **16**, 1942 (2016).
- [26] W. Möller, *Nucl. Instrum. Methods Phys. Res. Sect. B* **322**, 23 (2014).
- [27] T. S. Pugacheva, F. G. Djurabekova, and S. K. Valiev, *Nucl. Instrum. Methods Phys. Res. Sect. B* **141**, 99 (1998).
- [28] C. Fridlund, J. Laakso, K. Nordlund, and F. Djurabekova, *Nucl. Instrum. Methods Phys. Res. Sect. B* **409**, 14 (2017).
- [29] S. Munetoh, T. Motooka, K. Moriguchi, and A. Shintani, *Comput. Mater. Sci.* **39**, 334 (2007).
- [30] T. Watanabe, H. Fujiwara, H. Noguchi, T. Hoshino, and I. Ohdomari, *Jpn. J. Appl. Phys.* **38**, L366 (1999).
- [31] T. Watanabe, D. Yamasaki, K. Tatsumura, and I. Ohdomari, *Appl. Surf. Sci.* **234**, 207 (2004).
- [32] J. Samela and K. Nordlund, *Phys. Rev. B* **76**, 125434 (2007).
- [33] F. Djurabekova and K. Nordlund, *Phys. Rev. B* **77**, 115325 (2008).
- [34] A. A. Leino, S. L. Daraszewicz, O. H. Pakarinen, K. Nordlund, and F. Djurabekova, *Europhys. Lett.* **110**, 16004 (2015).
- [35] M. Backman, F. Djurabekova, O. H. Pakarinen, K. Nordlund, Y. Zhang, M. Toulemonde, and W. J. Weber, *J. Phys. D: Appl. Phys.* **45**, 505305 (2012).
- [36] J. F. Ziegler, J. P. Biersack, and U. Littmark, *The Stopping and Range of Ions in Solids* (Springer, Berlin, 1985).
- [37] J. Ziegler, see <http://www.srim.org> (2013).
- [38] H. J. C. Berendsen, J. P. M. Postma, W. F. van Gunsteren, A. DiNola, and J. R. Haak, *J. Chem. Phys.* **81**, 3684 (1984).
- [39] Ions4SET Project, <https://cordis.europa.eu/project/id/688072> (2019).
- [40] J. F. Ziegler, *Nucl. Instrum. Methods Phys. Res. Sect. B* **219**, 1027 (2004).
- [41] J. F. Ziegler, M. D. Ziegler, and J. P. Biersack, *Nucl. Instrum. Methods Phys. Res. Sect. B* **268**, 1818 (2010).
- [42] K. Nordlund, M. Ghaly, R. S. Averback, M. Caturla, T. Diaz de la Rubia, and J. Tarus, *Phys. Rev. B* **57**, 7556 (1998).
- [43] K. Nordlund, J. Keinonen, M. Ghaly, and R. S. Averback, *Nature* **398**, 49 (1999).
- [44] B. J. Cowen and M. S. El-Genk, *Comput. Mater. Sci.* **111**, 269 (2016).
- [45] J. Nord, K. Nordlund, and J. Keinonen, *Phys. Rev. B* **65**, 165329 (2002).
- [46] E. Salonen, K. Nordlund, J. Tarus, T. Ahlgren, J. Keinonen, and C. H. Wu, *Phys. Rev. B* **60**, R14005(R) (1999).
- [47] K. Nordlund, F. Djurabekova, and G. Hobler, *Phys. Rev. B* **94**, 214109 (2016).
- [48] T. S. Pugacheva, *Radiat. Eff.* **102**, 143 (1987).
- [49] A. Lopez-Cazalilla, A. Ilinov, L. Bukonte, K. Nordlund, F. Djurabekova, S. Norris, and J. Perkinson, *Nucl. Instrum. Methods Phys. Res. Sect. B* **414**, 133 (2018).
- [50] J. F. Ziegler, J. P. Biersack, and M. D. Ziegler, *SRIM: The Stopping and Range of Ions in Matter* (Cadence Design Systems, Raleigh, NC, 2008).
- [51] L. Bukonte, F. Djurabekova, J. Samela, K. Nordlund, S. A. Norris, and M. J. Aziz, *Nucl. Instrum. Methods Phys. Res. Sect. B* **297**, 23 (2013).
- [52] B. Weber, D. Stock, and K. Gärtner, *Nucl. Instrum. Methods Phys. Res. Sect. B* **148**, 375 (1999).
- [53] E. Snoeks, A. Polman, and C. A. Volkert, *Appl. Phys. Lett.* **65**, 2487 (1994).
- [54] R. Devine, *Nucl. Instrum. Methods Phys. Res. Sect. B* **91**, 378 (1994).
- [55] E. Snoeks, T. Weber, A. Cacciato, and A. Polman, *J. Appl. Phys.* **78**, 4723 (1995).
- [56] C. A. Volkert and A. Polman, *MRS Proc.* **235**, 3 (1992).
- [57] R. Devine, *J. Non. Cryst. Solids* **152**, 50 (1993).
- [58] A. Wootton, B. Thomas, and P. Harrowell, *J. Chem. Phys.* **115**, 3336 (2001).
- [59] P. Partyka, Y. Zhong, K. Nordlund, R. S. Averback, I. M. Robinson, and P. Ehrhart, *Phys. Rev. B* **64**, 235207 (2001).
- [60] K. Kyuno, D. G. Cahill, R. S. Averback, J. Tarus, and K. Nordlund, *Phys. Rev. Lett.* **83**, 4788 (1999).
- [61] S. O. Kucheyev, J. S. Williams, C. Jagadish, J. Zou, G. Li, and A. I. Titov, *Phys. Rev. B* **64**, 035202 (2001).
- [62] J. Nord, K. Nordlund, and J. Keinonen, *Phys. Rev. B* **68**, 184104 (2003).
- [63] J. Keinonen, F. Djurabekova, K. Nordlund, and K. P. Lieb, in *Silicon Nanophotonics: Basic Principles, Present Status and Perspectives* (World Scientific, Singapore, 2008), Chap. 14, pp. 379–396.